Controlling Sandwich-Structure of PET Microcellular Foams Using Coupling of CO_2 Diffusion and Induced Crystallization

Dachao Li, Tao Liu, Ling Zhao, and Weikang Yuan
State Key Laboratory of Chemical Engineering, East China University of Science and Technology,
Shanghai 200237, People's Republic of China

DOI 10.1002/aic.12764

Controlling sandwich-structure of poly(ethylene terephthalate) (PET) microcellular foams using coupling of CO_2 diffusion and CO_2-induced crystallization is presented in this article. The intrinsic kinetics of CO_2-induced crystallization of amorphous PET at 25°C and different CO_2 pressures were detected using in situ *high-pressure Fourier transform infrared spectroscopy and correlated by Avrami equation. Sorption of CO_2 in PET was measured using magnetic suspension balance and the diffusivity determined by Fick's second law. A model coupling CO_2 diffusion in and CO_2-induced crystallization of PET was proposed to calculate the CO_2 concentration as well as crystallinity distributions in PET sheet at different saturation times. It was revealed that a sandwich crystallization structure could be built in PET sheet, based on which a solid-state foaming process was used to manipulate the sandwich-structure of PET microcellular foams with two microcellular or even ultra-microcellular foamed crystalline layers outside and a microcellular foamed amorphous layer inside*. © 2011 American Institute of Chemical Engineers *AIChE J*, 58: 2512–2523, 2012

Keywords: PET microcellular foams, CO_2 diffusion, CO_2-induced crystallization, coupling, sandwich-structure

Introduction

Semicrystalline poly(ethylene terephthalate) (PET) is a low-cost engineering thermoplastics with good mechanical and thermal characteristics such as high elastic modulus, relatively high glass transition temperature (T_g) and good solvent resistance.[1] Besides for the production of fibers, films, trays, and bottles, PET was also applied for mechanical components and in some cases for replacement of commodity metals such as steel and aluminum.[2] In response to an industry challenge to reduce the amount of material used in plastic productions without sacrificing desirable mechanical properties, Suh et al.[3,4] proposed the concept of microcellular foam. The microcellular foams are defined as foams with cell size smaller than 10 μm. Unfortunately, the conventional melt process for producing microcellular foams, such as microcellular injection molding and extrusion foaming, are inadaptable for fabrication of PET foams from ordinary semicrystalline PET resins due to their low melt strength at processing temperatures. That is why in the past two decades, researches about preparation of microcellular foams focused mainly on amorphous polymers such as polystyrene,[5,6] poly (methyl methacrylate),[7] polysulfone,[8,9] and poly(ether imide).[10,11] Only a few studies have been conducted on the microcellular foaming of PET, and most of them are focused on the solid-state foaming, i.e., the foaming temperature is lower than the melting temperature of specific PET resin.[12–21]

As carbon dioxide (CO_2) has many unique properties such as nonflammable, nontoxic, relatively inexpensive, easy to reach a supercritical state (critical temperature, 31.1°C and critical pressure, 7.38 MPa), and relatively large solubility in polymers,[22,23] it has been used as a popular physical foaming agent in many foaming applications.[14,23–27] Dissolving CO_2 into polymers will affect their properties in both melt and solid states due to the so-called plasticization effect. It depresses the glass-transition temperature[28–30] and the crystallization temperature,[31] and changes the crystallization kinetics of several semicrystalline polymers.[31–33] Several studies of CO_2-induced crystallization have been reported for poly(aryl ether ether ketone), polycarbonate, poly(phenylene sulfide), and PET as well. Mizoguchi et al.[33] and Lambert and Paulaitis[32] investigated the CO_2-induced crystallization of amorphous PET at 35–80°C and 4–6 MPa, and compared it with thermal crystallization. They found that the crystallization took place even at temperatures below T_g measured in air due to the sorption of CO_2, and the crystallization rate at temperatures above T_g was greatly increased. However, the thermal properties from these studies were not *in situ* ones under high-pressure CO_2. The method adopted in these studies was to subject the polymer to a delay time between thermal characterization and pressurization, during which the polymer specimen was first enclosed in a high-pressure CO_2 chamber for a period of time to reach sorption equilibrium. Then, the specimen was taken out for further characterization after the CO_2 was released. Zhang and Handa[30] presented the *in situ* studies of PET thermal transitions under high-pressure CO_2 using high-pressure differential scanning calorimeter (DSC) and found that the absorbed CO_2

Correspondence concerning this article should be addressed to T. Liu at liutao@ecust.edu.cn or L. Zhao at zhaoling@ecust.edu.cn.

enhanced the mobility of the chain segments, depressed the crystallization temperature, and caused a lower T_g than room-temperature. However, it has been still impossible to study the kinetics of CO_2-induced crystallization of PET using this method due to the relatively slow crystallization rate of PET and poor signal-to-noise ratio of DSC in high-pressure CO_2 environment. In fact, the basic natures of CO_2-induced crystallization of semicrystalline PET at room-temperature, are far more complicated than we consider[34] because of the coupling effect of CO_2 diffusion and induced crystallization.[32] On the one hand, the presence of compressed CO_2 in PET matrix can enhance or increase the rate of crystallization. On the other hand, the rate of gas sorption in polymers can be coupled to additional kinetic phenomena, including the rates and extent of polymer swelling,[22] stress relaxation, and crystallization as well. The extent of crystallization in PET will affect gas permeability by reducing both the equilibrium solubility[13,32] and the diffusivity of gas in the polymer.[13,35] Hence, the kinetics of CO_2 sorption and induced crystallization are coupled with each other.[36]

The solid-state batch foaming process for producing PET microcellular foams was conducted by Baldwin et al.[13–15] The PET specimen was placed in a high-pressure vessel charged with CO_2, to a constant saturation pressure at room-temperature. Once the required saturation time was reached, the vessel was discharged. Then, the PET specimens were foamed, unconstrained, in a glycerin bath with certain temperature for the desired foaming time, and the specimens were quenched in a water bath to vitrify the microcellular structure. The cell morphology of the PET foams was found to be relevant to four major processing variables, i.e., gas saturation time, gas saturation pressure, foaming time, and temperature.[13] Crystallinity was found[13,37] to play a major role in the microcellular processing on (a) cell nucleation mechanisms resulting in larger cell densities due to heterogeneous nucleation at the amorphous/crystalline boundaries and (b) cell growth mechanisms resulting in smaller cell sizes due to the increased stiffness of the semicrystalline matrix. Kumar[12] used the solid-state foaming process combining with the CO_2-induced crystallization to produce PET foams with integral crystalline skin, i.e., a foamed core layer with unfoamed crystalline skins. This structure exhibited enhanced physical properties compared to conventional PET foams. The largest drawback of this batch foaming method was time consuming due to the long saturation time. Kumar et al.[16,17] successfully converted this batch process into a semicontinuous process which allowed essentially continuous production of microcellular foams. PET foams, nowadays, have been successfully commercialized and used in applications such as packaging, thermal insulation, optical reflection, and preferable sandwich materials in wind energy, marine and transportation.[12,38–41]

In this work, we decoupled the complicated relationships between CO_2 diffusion in and CO_2-induced crystallization of amorphous PET. The intrinsic kinetics of CO_2-induced crystallization of amorphous thin PET films (15 ± 2 μm) were detected at 25°C and different CO_2 pressures using *in situ* high-pressure Fourier transform infrared spectroscopy (FTIR). Magnetic suspension balance (MSB) was used to determine the solubility and diffusivity of CO_2 in PET matrix. A model coupling the CO_2 diffusion and induced crystallization was subsequently proposed to correlate and predict the CO_2 concentration distribution as well as the crystallinity distribution in the PET matrix at different saturation time. On the basis of the modeling results, a solid-state foaming process was used to manipulate sandwich-structure of PET microcellular foams with two microcellular or even ultra-microcellular foamed crystalline layers outside and a microcellular foamed amorphous layer inside. The thickness of the foamed crystalline layer agreed well with that calculated by the model.

Experimental

Materials

PET (BRH-400) with intrinsic viscosity of 1.0 dl/g (corresponding viscosity average molecular weight $\overline{M}_v$ = 42,000 g/mol) was kindly provided by Shanghai Petrochemical Co. The crystallinity and melting temperature of the PET were 32.8% and 255°C, which were determined by DSC (NETZSCH DSC 204 HP, Germany) under atmospheric N_2. Before being used, the PET pellets were dried in a vacuum oven at 80°C for 8 h to eliminate moisture. CO_2 (purity: 99.9%, w/w) was purchased from Air Products Co. (Shanghai, China).

In situ *high-pressure FTIR*

The amorphous PET films were prepared from pellets using a hot press at 280°C and 10 MPa for 5 min and rapidly quenched by plunging into cold water. The film thickness measured by micrometer caliper was 15 ± 2 μm. Compared with crystallization time, the CO_2 diffusion time (or saturation time) in such thin film could be negligible. Therefore, it was assumed that the film was saturated as soon as the high-pressure CO_2 was applied, and the obtained crystallization kinetics should be intrinsic kinetics. The intrinsic kinetics of the CO_2-induced crystallization of the amorphous PET films at 25°C and high CO_2 pressures was investigated using *in situ* FTIR of type Bruker Equinox-55 equipped with a Harrick high-pressure demountable cell, the details of which had been described elsewhere.[42] The FTIR spectra were recorded at a resolution of 2.0 cm^{-1} and a rate of one spectrum per 10 min. The IR intensities refer to the peak height. The scanned wave number was in the range of 4000–400 cm^{-1}.

Magnetic suspension balance

Melting of PET was performed in a Haake Minilab system (Thermo Electron Co.) under 0.6 MPa nitrogen atmosphere at a temperature of 280°C and a screw speed of 50 rotations/min. The melts were then delivered into a Haake Minijet system (Thermo Electron Co.) and molded into PET sheets with geometry of 30 × 15 × 1.2 mm at a pressure of 650 bar and mold temperature of 50°C. The molded amorphous PET sheets were used for the solubility and diffusivity measurements and foaming experiments.

The solubility and diffusivity of CO_2 in PET was measured using MSB (Rubotherm Prazisionsmesstechnik GmbH, Germany). The MSB has an electronically controlled magnetic suspension coupling that transmits the weight of the sample in a pressure vessel to a microbalance outside of the cell. The MSB can be used at pressures up to 35 MPa and temperatures up to 523 K. Resolution and accuracy of the microbalance (Mettler AT261, Switzerland) are 0.01 mg and 0.002%, respectively. The system temperature and pressure was controlled at the accuracy of ±0.2°C and ±0.05 MPa, respectively. Density of carbon dioxide needed for buoyancy correction was measured simultaneously by MSB. The most important advantage of MSB method was that it could accurately detect the mass variation of polymer sample during gas sorption process. The original sample volume was determined by a blank test with Helium and used to correct the gas solubility by considering gas buoyancy acting on the polymer. Details of the MSB apparatus and experimental procedure used in this work have been described in previous publications.[43–46]

Foaming process

A so-called temperature rising foaming process was used to fabricate PET microcellular foams. The amorphous PET sheets were placed in a high-pressure vessel. The latter was then sealed, carefully washed with low-pressure CO_2 and charged with 6 MPa CO_2. Thereafter, the vessel was immersed into a water bath with a constant temperature of 25°C. Different saturation time ranging from a few hours to as long as 15 days was applied to the PET sheets. After that, the PET sample was taken out and immediately immersed, without constraint, into a high-temperature silicone oil bath with a temperature of 235°C to induce bubble nucleation and growth. After a foaming time of 10 s, the samples were quenched in an ice-water bath to vitrify the foam structure.

Foam characterization

The cell morphologies of the PET foams were characterized by a JSM-6360LV (JEOL Tokyo, Japan) scanning electron microscopy (SEM). The samples were immersed in liquid nitrogen for 10 min and then fractured. The SEM scanned fractured surfaces with Pd (palladium) coating. The average cell size was obtained through the analysis of the SEM photographs by the software of Image-Pro Plus (Media Cybernetics, Silver Spring, MD). The number average diameter of all the cells in the micrograph, d, was calculated using the following equation

$$d = \frac{\sum d_\mathrm{i} n_\mathrm{i}}{\sum n_\mathrm{i}} \tag{1}$$

where n_i is the number of cells with a perimeter-equivalent diameter of d_i. The mass densities of foamed PET samples ρ_f were measured according to ASTM D792-00, involving weighing polymer foam in was using a sinker. ρ_f was calculated as follows

$$\rho_\mathrm{f} = \frac{a}{a + w - b}\rho_\mathrm{water} \tag{2}$$

where a is the apparent mass of specimen in air without sinker, b the apparent mass of specimen and sinker completely immersed in water, and w is the apparent mass of the totally immersed sinker. The volume expansion ratio of the PET foams, R_v, is defined as the ratio of the bulk density of the virgin PET (ρ_0) to that of the foamed one (ρ_f)

$$R_\mathrm{v} = \frac{\rho_0}{\rho_\mathrm{f}} \tag{3}$$

The cell density (N_0), the number of cells per cubic centimeter of foamed PET was determined from the equation

$$N_0 = \left[\frac{nM^2}{A}\right]^{3/2} \tag{4}$$

where n is the number of cells in the SEM micrograph, M is the magnification factor, and A is the area of the micrograph (in cm^2).

Results and Discussion

Intrinsic kinetics of CO_2-induced PET crystallization

A number of studies have been done on the IR spectroscopy characterization of contributing conformers of PET chains.[47–49] The $\text{—O—CH}_2\text{—CH}_2\text{—O—}$ moiety of a PET chain shows gauche and trans conformers through the internal rotation of the COC bond. In the crystalline phase, the $\text{—O—CH}_2\text{—CH}_2\text{—O—}$ moiety adopts a trans conformation. Whereas in the amorphous phase, it is mainly in the gauche conformation with some small contribution of the trans conformation.[49] Therefore, the crystallinity of PET can be estimated. In the IR spectrum of PET, the 1340 and 1370 cm^{-1} band are assigned to the CH_2 wagging mode in the trans and gauche conformers, respectively. As the intensities of these two bands are comparable in the spectrum of amorphous PET, we chose these two bands as the key bands for determining the relative conformational population. The crystallinity, I, of PET can be estimated as follows

$$I = A_{1340}/(A_{1340} + 6.6 \times A_{1370}) \tag{5}$$

where A_{1340} and A_{1370} were the integral absorbance of the 1340 and 1370 cm^{-1} bands, respectively. The factor 6.6, describing the absorption coefficient ratio of 1340 and 1370 cm^{-1},[50] had been obtained from the slope of a plot of the integral absorbance of the1340 cm^{-1} band vs. that of the 1370 cm^{-1} band according to the spectra of PET samples with different crystallinity. This method had been used in the crystallinity determination of bulk PET[40] and PET thin film.[49]

The *in situ* high-pressure FTIR spectra of the PET film during isothermal crystallization induced by CO_2 at 25°C and different pressures are shown in Figure 1. As the crystallization time was prolonged, the absorbance of the 1340 cm^{-1} band grew, whereas the absorbance reduction of the 1370 cm^{-1} band was relatively small. This was attributed to the difference in the absorption coefficients of these two bands. Figure 2 shows the variation of the crystallinity I of the PET films with the crystallization time under different pressure CO_2 during isothermal crystallization at 25°C. It was shown that no crystallinity increase could be detected under 4.5 MPa CO_2 even after 2000 min, while a very long crystallization period of more than 1500 min was observed under 5.0 MPa CO_2. These results indicated that the least critical pressure, corresponding to the least critical CO_2 concentration in the PET, for CO_2-induced crystallization of PET was 5.0 MPa at the temperature of 25°C. The crystallization rate of PET film increased rapidly with increasing saturation CO_2 pressure, and the final crystallinity was also a little bit higher at the higher saturation CO_2 pressure.

The well-known Avrami equation,[51–53] which provided an insight into the progress of nucleation and crystal growth that occurred during isothermal crystallization, was used to study the isothermal CO_2-induced crystallization kinetics of PET films.[49,54–56] The Avrami equation is in the form as

$$1 - X_t/X_\infty = \exp(-Kt^n) \tag{6}$$

where X_t is the crystallinity of the sample at time t, X_∞ the crystallinity at which a further increase in the crystallinity with time is imperceptible, K a constant that includes the rate constants of growth and nucleation, and n is the Avrami exponent with a value between 1 and 4. We adopted the Avrami equation to fit our results as follows

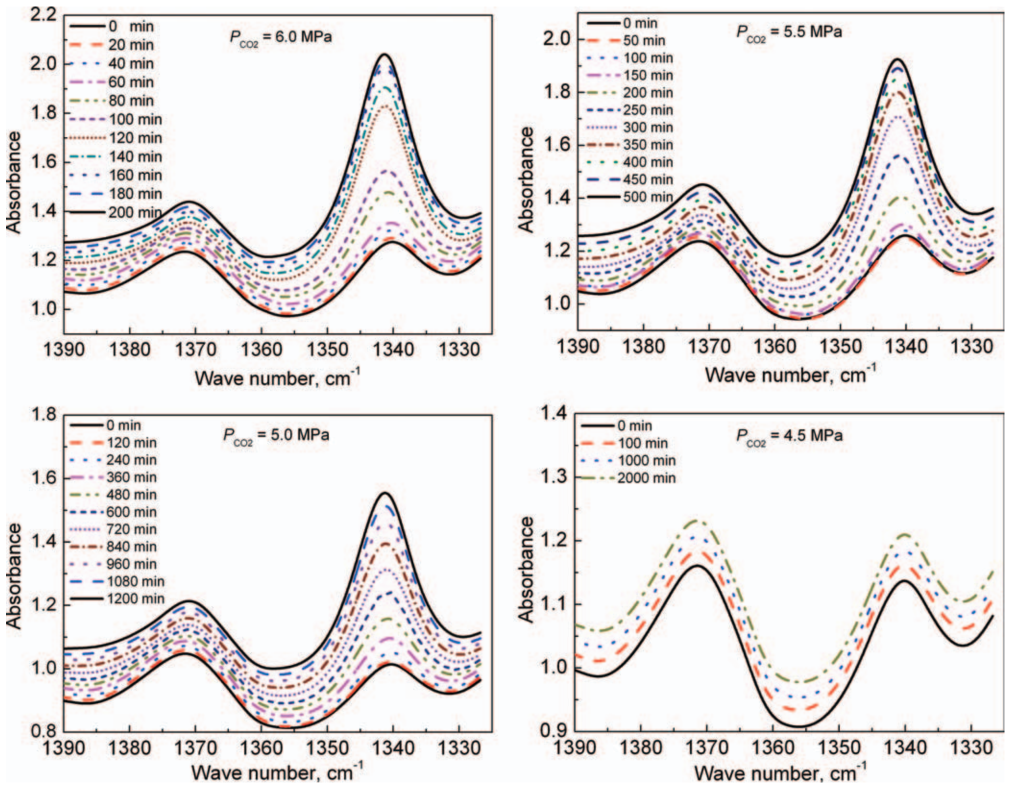

Figure 1. High-pressure FTIR spectra in the 1320–1390 cm^{-1} region of the PET film at different crystallization times during isothermal crystallization at 25°C and different CO$_2$ pressures.

[Color figure can be viewed in the online issue, which is available at wileyonlinelibrary.com.]

$$X_t/X_\infty = (I_t - I_0)/(I_\infty - I_0) \tag{7}$$

where I_0, I_t, and I_∞ are the fractions of the trans conformers at the beginning of crystallization, at time t, and at later periods when a further increase is imperceptible, respectively.

Taking double logarithms, Eq. 6 then becomes

$$\ln[-\ln(1 - X_t)] = n \ln t + \ln K \tag{8}$$

Avrami plots of the isothermal crystallization of PET films induced by different pressure CO$_2$ at 25°C are shown in Figure 3. The relatively crystallinity ranging from 10 to 95%, i.e., $\ln[-\ln(1 - X_t)]$ from -2.2 to 1.1, was selected for the analysis. When the relatively crystallinity was lower than 95%, the growth of spherulites could be considered as independently and there was barely any interaction or contact between adjacent spherulite during growth. In this case, Avrami equation could perfectly describe the growth of spherulite and the linear behavior could be obtained as shown in Figure 3. When the relatively crystallinity was larger than 95%, due to the limitation of growing space, the contact and interaction between adjacent spherulite would be inevitable and a nonlinear behavior or inflection point would be observed. The half-crystallization time, $t_{1/2}$, defined as the time at which the relative crystallinity is 50 wt %, can be determined either from the experiment directly or from the obtained crystallization kinetic parameters as follows

$$t_{1/2} = \left(\frac{\ln 2}{K}\right)^{1/n} \tag{9}$$

The calculated Avrami exponent, n, and crystallization rate constant, K, from Eq. 8, as well as both calculated and experimental half-crystallization time, $t_{1/2}$, at different CO$_2$ pressures were given in Table 1. The physical interpretation of the Avrami exponent, n, is the dimension of crystal growth. For homogeneous nucleation, like in our case, the value of n equal to 2, 3, or 4 represents the one-, two-, or three-dimension (3-D) growth of crystals, respectively. As the saturation pressure varied from 5 to 6 MPa, the value of n increased from 2.94 to 3.71, which suggested that the way of crystal growth converted from 2-D dominated to 3-D dominated with

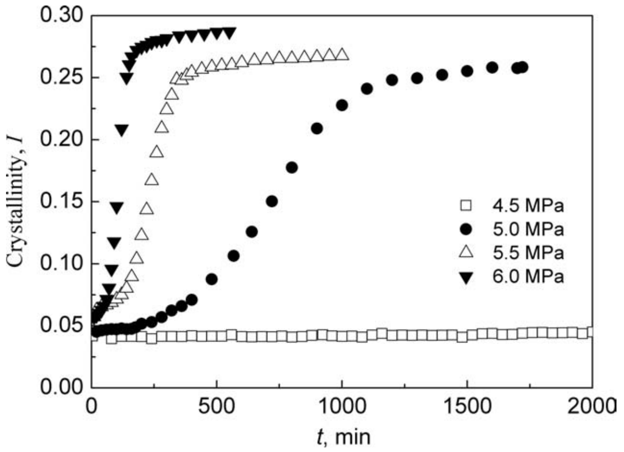

Figure 2. Changes in crystallinity of PET films during isothermal crystallization at 25°C and different CO$_2$ pressures.

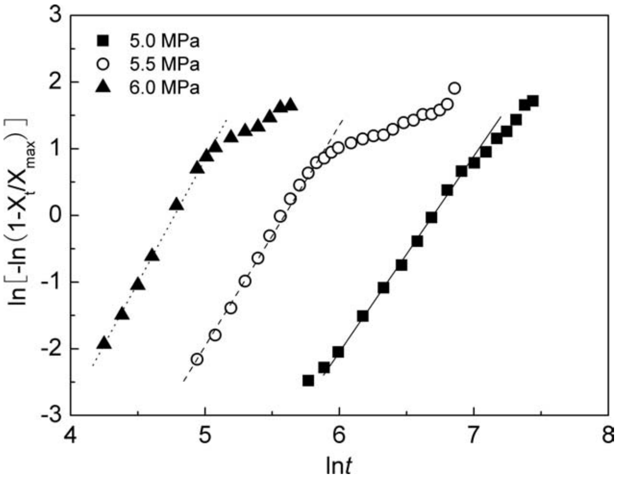

Figure 3. Avrami plots of the isothermal crystallization of PET films induced by different pressure CO_2 at 25°C.

increasing CO_2 pressure. This observation was reasonable because the molecular chain of the PET could have more mobility under higher-pressure CO_2 due to the plasticization effect. The crystallization rate constant, K, at 6 MPa was almost one magnitude higher that of 5 MPa, which significantly reduced the half crystallization time from 720 to 109 min. The consistency between calculated and experimental half-crystallization time suggested that the Avrami equation could well describe the CO_2-induced crystallization behavior of PET.

Solubility and diffusivity of CO_2 in the PET at 25°C

The MSB method was adopted to investigate the solubility and diffusivity of CO_2 in the PET sheet at 25°C and 6 MPa. Figure 4a shows the CO_2 mass uptake in the PET sheet at 25°C and 6 MPa after buoyancy correction of MSB method. Details about buoyancy correction of MSB method had been described elsewhere.[43–46] As CO_2 diffused into the PET matrix, distribution of CO_2 concentration was founded and varied with saturation time. The CO_2-induced crystallization took place where the CO_2 concentration was high enough. Therefore, the layers near the sheet surface crystallized earlier. The formation of crystals would subsequently reject CO_2 and decrease the CO_2 content in the PET matrix. Thus, there were two main factors affecting the solubility: one was the CO_2 diffused in the PET matrix before the equilibrium state reached, which would increase the CO_2 content; the other was CO_2-induced crystallization, which would reject CO_2. Before the sorption curve reached the ‘‘peak’’ value of the knee, the sorption speed was larger than the rejection speed, and the PET matrix was absorbing CO_2 as a whole. As the sorption curve passed through the knee (i.e., peak value), the sorption speed was passed over by the rejection speed, and the CO_2 content in the whole PET matrix began to decrease and finally reached an equilibrium value when crystallization completed.

Table 1. *n* and *K* Values, and Half Crystallization Time of the PET Film at Different CO_2 Pressures

T (°C)	P (MPa)	n	K	$t_{1/2}$ (min; Experimental)	$t_{1/2}$ (min; Calculated)
25	5.0	2.94	2.81×10^{-9}	720	715
	5.5	3.32	8.96×10^{-9}	238	246
	6.0	3.71	2.07×10^{-8}	109	107

As shown in Figure 4a, the equilibrium solubility of CO_2 in the whole PET sheet, S, was determined to be 78.7 g/kg PET, while the crystallinity of the PET sample after MSB measurement was determined to be 28.6% by DSC. Assuming the solubility of CO_2 in crystalline regions of polymer is zero, which has been widely accepted,[22,44] the saturation concentration, C_0, of CO_2 in amorphous regions of the PET at 25°C and 6 MPa can be determined to be 11.0 wt % with the following equation

$$C_0 = \frac{S/1000}{1 - X_\infty} \times 100\% \tag{10}$$

where S is the equilibrium solubility of CO_2 in the whole PET specimen at 25°C and 6 MPa and X_∞ is crystallinity of the PET sample after MSB measurement.

The least critical CO_2 concentration, C_{critical}, i.e., equilibrium concentration of CO_2 in amorphous PET under 5 MPa CO_2, for induced crystallization of PET at 25°C was estimated to be 9.17 wt % assuming the sorption of CO_2 could be expressed by the Henry’s law at relatively low CO_2 pressure.

Assuming that the diffusion could be expressed by Fick’s second law

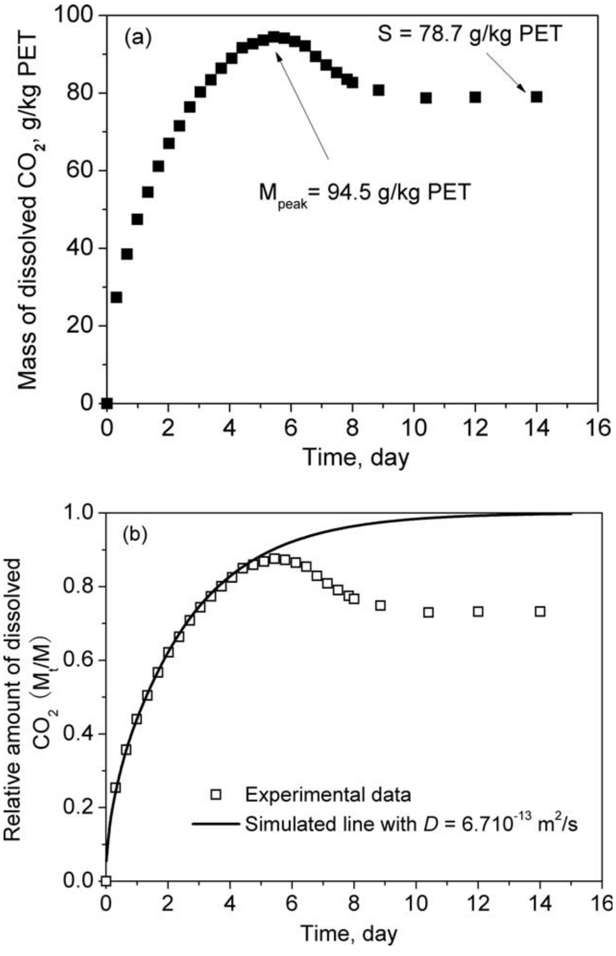

Figure 4. Sorption profiles for CO_2 in PET at 25°C and 6 MPa.

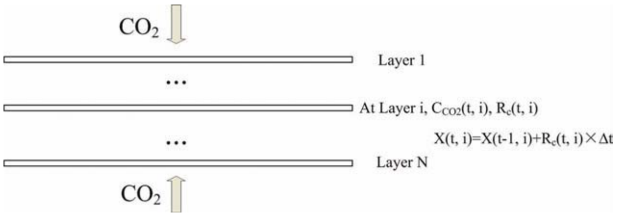

Figure 5. Schematic diagram of the proposed model.

[Color figure can be viewed in the online issue, which is available at wileyonlinelibrary.com.]

$$\frac{\partial C}{\partial t} = D\frac{\partial^2 C}{\partial x^2} \tag{11}$$

Because the other 2-D of the PET sheet were more than 10 times larger than the thickness, CO_2 entered effectively through the plane faces and a negligible amount through the edges. Thus, the diffusion process could approximately be treated as 1-D diffusion in an infinite sheet with constant surrounding concentration, i.e., constant surface concentration. The correspondingly initial and boundary conditions in this case were

$$\begin{aligned} C &= 0, && \text{at } -l < x < l, t = 0, \\ C &= C_0, && \text{at } x = l, t \geq 0, \\ C &= C_0, && \text{at } x = -l, t \geq 0 \end{aligned}$$

where C is the concentration of CO_2 in PET, $2l$ is the thickness of PET sheets and D is the diffusion coefficient of CO_2 in the polymer, which was treated as being independent on the gas concentration during gas dissolution. The appropriate solution of the diffusion equation had been given by Crank[57]

$$\frac{M_t}{M_\infty} = 1 - \sum_{n=0}^{\infty} \frac{8}{(2n+1)^2\pi^2} \exp\left[\frac{-D(2n+1)^2\pi^2 t}{4l^2}\right] \tag{12}$$

where M_t and M_∞ are the mass of dissolved gas in the polymer at $t = t$ and $t = \infty$, respectively.

In fact, the obtained ''knee-like'' sorption profile was not a typical Fick diffusion. Thus, Eq. 12 could not be used to describe the whole sorption process. As stated above, this sorption process could be divided into sorption dominated step and crystallization dominated step. Before the sorption curve reached the peak value of the knee, the diffusion process was dominated by the sorption of CO_2 into PET matrix. Thus, the sorption data from $t = 0$ to $t = t_{\text{peak}}$, the time sorption reached the peak value, was adopted to correlate the diffusion coefficient with Eq. 12. M_∞ in Eq. 12 was determined by the solubility of CO_2 in amorphous PET at this condition, i.e., C_0. As shown in Figure 4b, the obtained diffusion coefficient at the experimental condition was 6.7×10^{-13} m^2/s with an average relative deviation of 1.8%. Note that this value was six to eight times larger than those typically reported for the diffusivity of lower-pressure (no more than 1 MPa) CO_2 in PET matrix.[58,59] This was because the T_g of PET under low-pressure CO_2 was still higher than the experimental temperature, i.e., 25°C, the molecular chain of PET could not move and the specimen could not be swollen by CO_2. While in our case, the T_g of PET under 6 MPa CO_2 was lower than 25°C, otherwise the induced crystallization could not happen, and the PET sample could be swollen by CO_2. It had been reported that the dissolution of CO_2 in polymer matrix would induce the polymer swelling and increase the free volume so as to lead a dramatically increase in diffusion coefficient.[13,22,43]

Modeling of the coupling of CO_2 diffusion in and induced crystallization of PET

What we concerned about was: after a certain saturation time, the CO_2 concentration and crystallinity distributions in the PET sheet. To investigate the coupling process of CO_2 diffusion in and induced crystallization of the PET sheet, a model was proposed as shown in Figure 5. Assuming that the PET sheet was consisted of N well-contacted layers in the thickness direction, the thickness of each layer was equal and so small that the CO_2 concentration distribution was uniform in each individual layer. A few assumptions were further made:

(1) The diffusion of CO_2 in the PET sheet could be expressed by Fick's second law;

(2) The CO_2 concentration distribution was uniform in each individual thin layer;

(3) The CO_2 concentration and the rate of CO_2 induced crystallization in an individual thin layer were constant in a short time (e.g., 1 min);

(4) Crystallinity of PET sheet had no effect on the diffusion coefficient.

In such case, the concentration of CO_2 in each layer could be determined by the following equation[57]

$$\frac{C(t,i)}{C_0} = 1 - \frac{4}{\pi}\sum_{n=0}^{\infty} \frac{(-1)^n}{2n+1} \exp\left[\frac{-D(2n+1)^2\pi^2 t}{4l^2}\right] \times \cos\frac{(2n+1)\pi x(i)}{2l} \tag{13}$$

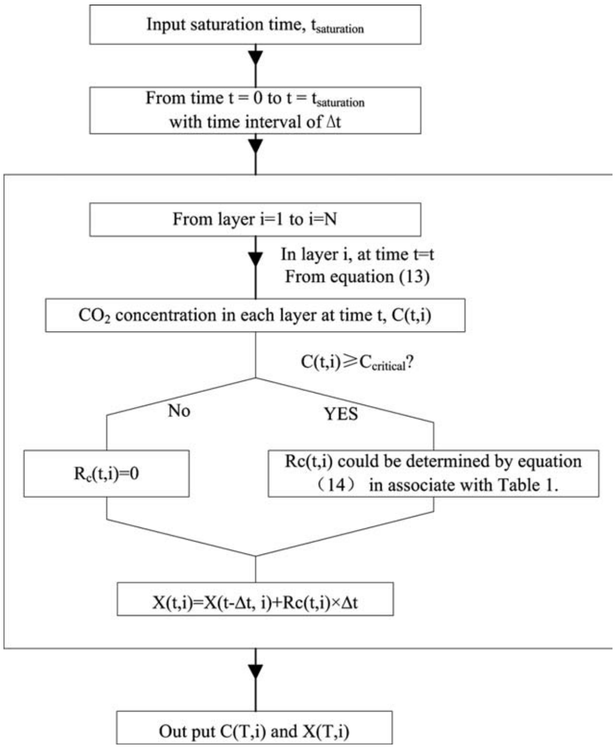

Figure 6. Calculation flow chart of the proposed model.

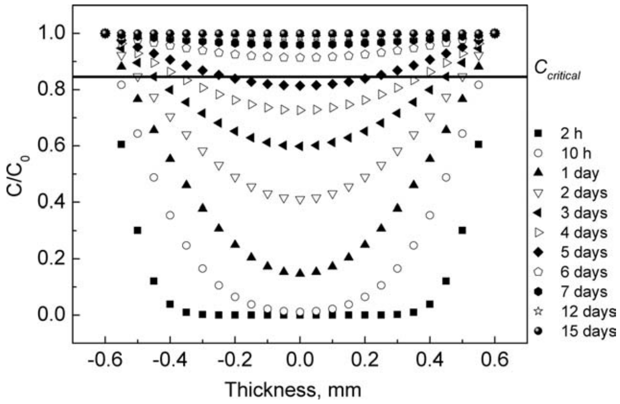

Figure 7. CO_2 concentration distribution in the PET sheet at different saturation time under 6 MPa CO_2.

where $C(t, i)$ is the concentration of CO_2 at saturation time t in layer i, $x(i)$ is the location of layer i in the thickness direction of the PET sheet, and D is the diffusion coefficient, which had been determined to be 6.7×10^{-13} m^2/s.

The crystallization rate, R_c, in each individual layer could be determined by the differential form of Eq. 6

$$R_c = \frac{dX_t}{dt} = Kt^{n-1}\exp(-Kt^n) \tag{14}$$

where n and K are the Avrami exponent and crystallization rate constant, respectively. The flow chart of the simulation process was shown in Figure 6.

Evolution of CO_2 concentration distribution and CO_2-induced crystallinity distribution against saturation time were shown in Figures 7 and 8, respectively. Because of the relatively small diffusion coefficient of CO_2 in the PET sheet at the experimental condition, the saturation process should take as long as 15 days to approach the equilibrium state (99% saturation). CO_2-induced crystallization could only occur at those positions where the CO_2 concentration was higher than C_{critical}, i.e., $C/C_0 \geq C_{\text{critical}}/C_0 = 0.833$. While after CO_2 concentration exceeded C_{critical}, it would still take ~1 day to complete the crystallization process, which was determined by the crystallization kinetics discussed above. Thus, in the first few days of saturation, the evolution of CO_2-induced crystallization was pretty slow. For example, after 4 days' saturation, the thickness of crystallized layer was still no more than 0.15 mm. As shown in Figure 7, the CO_2 concentration was higher than C_{critical} in most part of the PET sheet after 5 days' saturation, and higher than C_{critical} in the whole PET after 6 days. Corresponding evolution rate of crystallinity from day 5 to 6, as shown in Figure 8, was much faster than that in the first 4 days. The

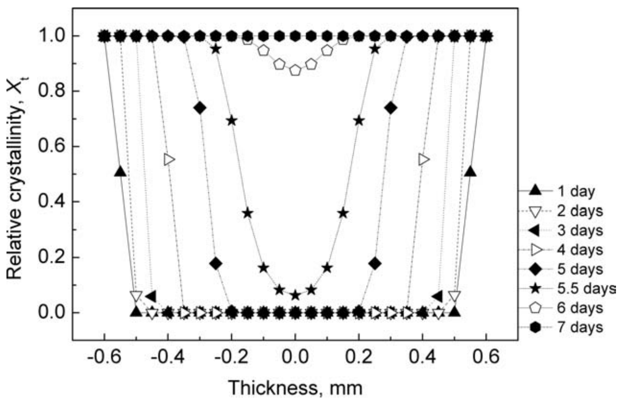

Figure 8. Crystallinity distribution in the PET sheet at different saturation time under 6 MPa CO_2.

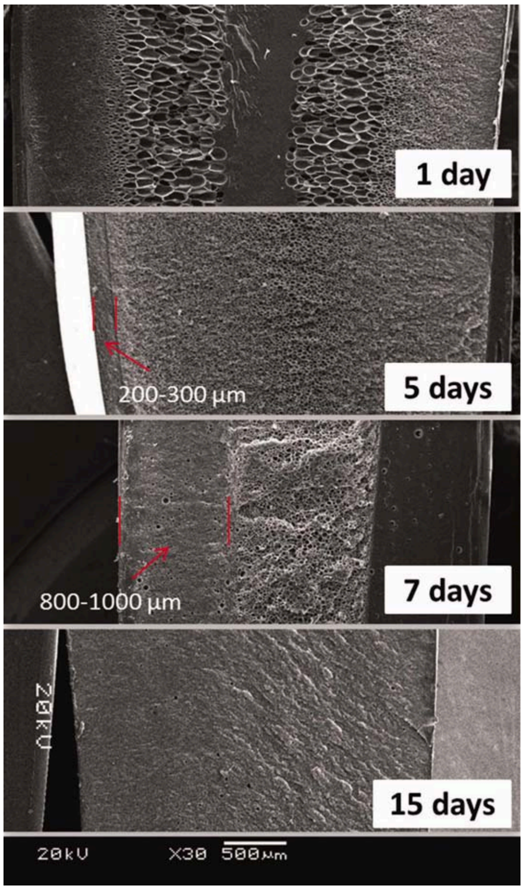

Figure 9. The overall bubble morphology of PET foams prepared with different saturation times.

[Color figure can be viewed in the online issue, which is available at wileyonlinelibrary.com.]

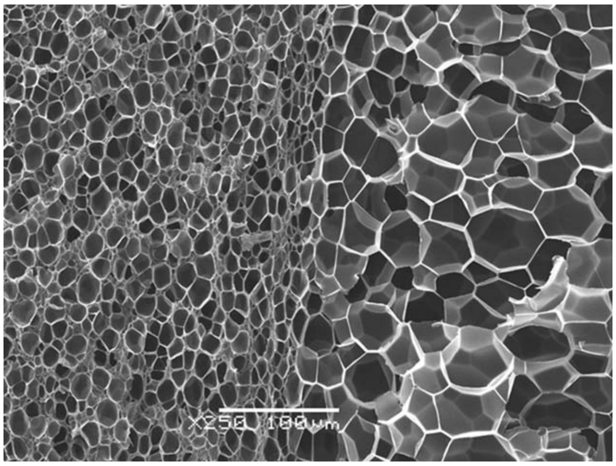

Figure 10. Typical boundary between the crystalline layer and the amorphous layer of the PET foam.

crystallization process in the whole PET sheet completed after 7 days' saturation.

From the crystallinity distribution profile after different saturation time, as shown in Figure 8, it was interesting to find that a "sandwich" crystallization structure could be built after an appropriate saturation time, e.g., 4 or 5 days. This structure was resulted from the rate difference between CO_2 diffusion and induced crystallization, i.e., the coupling effect of them. Because of the different foaming behaviors of amorphous PET and crystalline PET,[13–15,18] it was highly possible to control a sandwich foaming morphology using the obtained sandwich crystallization structure.

Controlling of sandwich-structure of PET microcellular foams

A so-called temperature rising foaming process was conducted to fabricate PET microcellular foams with sandwich structure using the coupling effect of CO_2 diffusion and induced crystallization of PET. Kumar et al.[17] used the "temperature rising" foaming process to produce high relative density PET microcellular foams using CO_2 as a blowing agent. Their samples were saturated at room-temperature and elevated CO_2 pressures, and then foamed at temperatures ranging from 50 to 90°C. In this work, we adopted a foaming temperature as high as 235°C, which was just 20°C lower than the melting temperature of the PET. There are two reasons for choosing this high foaming temperature: one was that higher foaming temperature would create larger thermodynamic instability, which was favorable for bubble nucleation and the other was that the difference between foaming morphologies of crystalline layer PET and amorphous layer PET could be more obvious at higher foaming temperature.

The overall morphology of PET foams prepared with different saturation times were shown in Figure 9. The evolution of foam morphology could be easily understood if considered combining with Figures 7 and 8. When the saturation time was just 1 day, most parts of the PET sheet were still unsaturated, and CO_2 concentration decreased rapidly from the surface to the central area. Relatively small cell size and high cell density were obtained in the areas near the surface, while a sharp decrease of cell density and increase of cell size could be observed in the areas near the center, and the central part of the PET sheet was unfoamed. After 5 days' saturation, as shown in Figure 7, the distribution of CO_2 concentration had been relatively uniform in the PET sheet, which led to uniform cell morphology in most areas of the sample. Amazingly, a thin layer with fine cells was observed near the surface. Foams morphology between the thin layer and inner part of the PET sheet were shown in Figure 10. Crystallinity was found[13,37] to play a major role in the microcellular processing on (a) cell nucleation mechanisms resulting in larger cell densities due to heterogeneous nucleation at the amorphous/crystalline boundaries and (b) cell growth mechanisms resulting in smaller cell sizes due to the increased stiffness of the semicrystalline matrix. Thus, observation of the thin layer with fine cells indicated the formation of CO_2-induced crystallization layer, which was coincident with the simulation result shown in Figure 8. When the saturation time increased from 5 to 7 days, the thickness of the crystalline layer increased dramatically as shown in Figure 8, and the foaming experiment also confirmed it. The thickness of the crystalline layer (after foaming) increased from 250 to 900 μm. After saturation time as long as 15 days, both CO_2 diffusion and induced crystallization completed, and the foams' morphology was quite uniform all through the PET sheet.

Time	Panoramic	Amorphous Layer	Boundary	Crystalline Layer
1 day	Figure11–1(a)	Figure11–1(b)	No	No
2 days	Figure11–2(a)	Figure11–2(b)	Figure11–2(c)	Figure11–2(d)
3 days	Figure11–3(a)	Figure11–3(b)	Figure11–3(c)	Figure11–3(d)
5 days	Figure11–4(a)	Figure11–4(b)	Figure11–4(c)	Figure11–4(d)
7 days	Figure11–5(a)	Figure11–5(b)	Figure11–5(c)	Figure11–5(d)
12 days	Figure11–6(a)	Figure11–6(b)	No	Figure11–6(d)
15 days	Figure11–7(a)	No	No	Figure11–7(d)

Details about the evolution of the crystalline layer against saturation time were shown in Figure 11. No crystalline layer could be observed after 1 day's saturation, because barely any crystalline layer could form during such a short saturation time, as shown in Figure 8. When the saturation time was longer than 2 days, a foamed layer with smaller bubble size and larger bubble density could be observed near the skin of PET foam, indicating the formation of crystalline layer. The boundary of crystalline layer and amorphous layer after foaming was also clearly shown in Figure 11. Coincident with Figure 8, the thickness of crystalline layer increased with saturation time. When the saturation time was longer than 7 days, due to completion of the CO_2-induced crystallization, the foaming morphology became uniform. Interestingly, the saturation time as long as 15 days further improved the perfection of CO_2-induced crystallization of the PET sheet, and an ultra-microcellular structure with cell size distribution as small as 100–300 nm was obtained.

The thicknesses of the crystalline layers calculated using the model coupling CO_2 diffusion and induced crystallization, as well as those measured from the PET foams, at different saturation time were shown in Table 2. Basically, the model could well predict the evolution of crystalline layer against different saturation time. When the saturation time was relatively short, i.e., short than 3 days, the thickness of crystalline layers in the PET foams was slightly larger than that predicted from the model, which was due to the expansion of crystalline layer during foaming experiment. While at relatively long saturation time, e.g., 5 or 7 days, the evolution of crystalline layer in the PET foams was slower than that from the modeling. In the model assumption, it was assumed that the crystallization of PET had no effect on the diffusion coefficient, but in fact, CO_2-induced crystallization of PET would reduce the free volume of samples and extend the path of CO_2 diffusion. These effects would decrease the

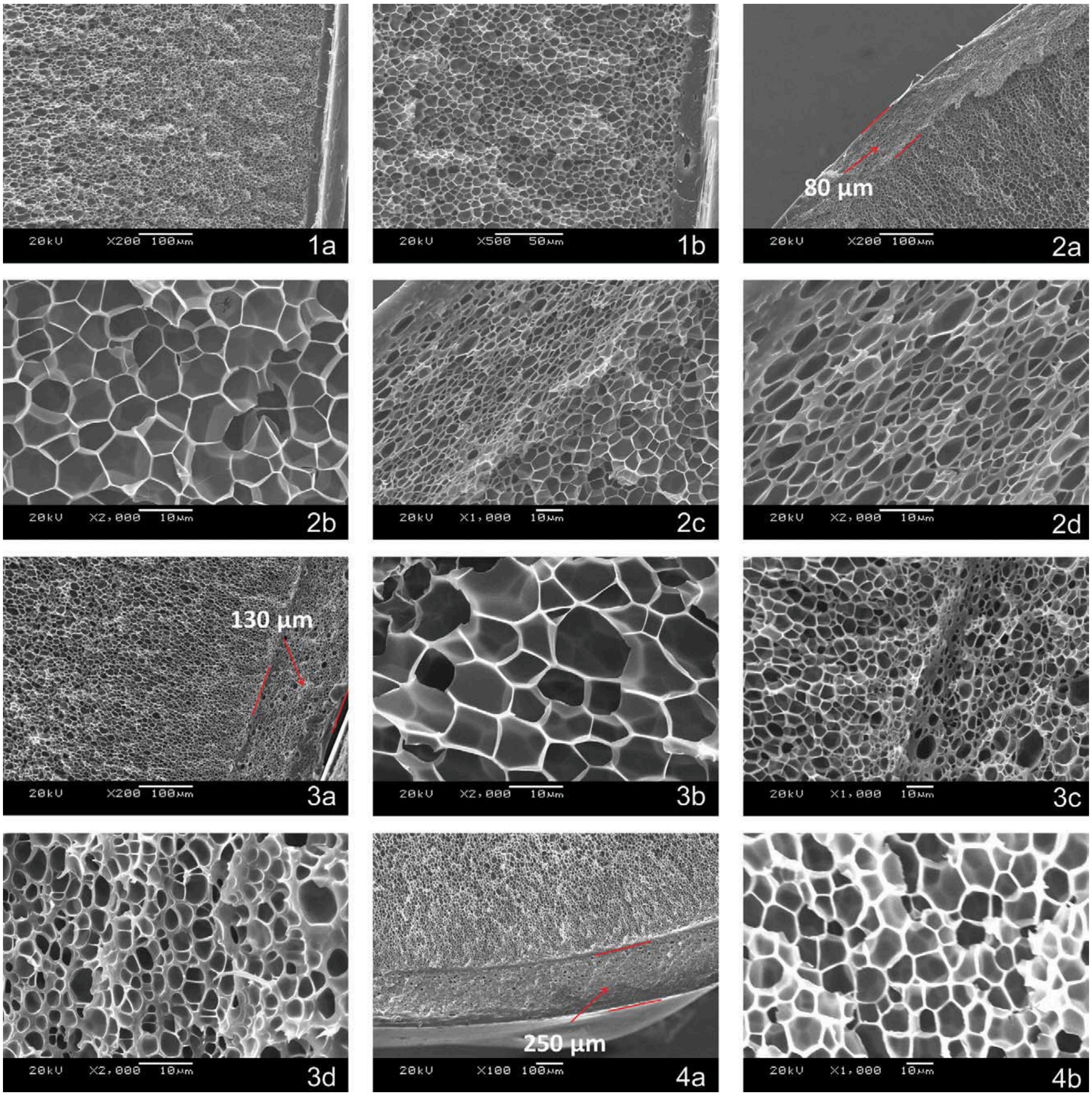

Figure 11. Evolution of foaming morphology of different areas of the PET foams against saturation time.

[Color figure can be viewed in the online issue, which is available at wileyonlinelibrary.com.]

diffusion coefficient of CO_2 to some extent and delay the evolution of crystalline layer.

The evolution of bubble size and bubble density of both crystalline and amorphous layers, and expansion ratio in the PET foams against saturation time is shown in Figure 12. Because of the increase of CO_2 concentration with increasing saturation time in the amorphous layer of the PET specimen, more CO_2 was available to support the bubble growth, which led to an increase in both bubble size and expansion ratio within the saturation time of 5 days. When the saturation time was longer than 7 days, as revealed by the model, the crystal structure of the crystalline became more perfect, and small amount of crystals could have formed in the amorphous layer. Existence of crystal regions in PET matrix restricted the bubble growth, and changed the bubble nucleation mechanism from homogeneous nucleation to heterogeneous one, which dramatically reduced the activation energy of bubble nucleation and greatly increased the bubble density of PET foams. Especially at the saturation time of 15 days, ultra-microcellular PET foams with average bubble size as small as 193 nm and bubble density as large as 3.37×10^{13} were obtained.

Conclusion

In this work, the intrinsic kinetics of CO_2-induced crystallization of amorphous PET at 25°C and different CO_2 pressures were detected using *in situ* high-pressure FTIR and correlated by Avrami equation. The least critical CO_2 pressure, at which CO_2-induced crystallization could occur, was

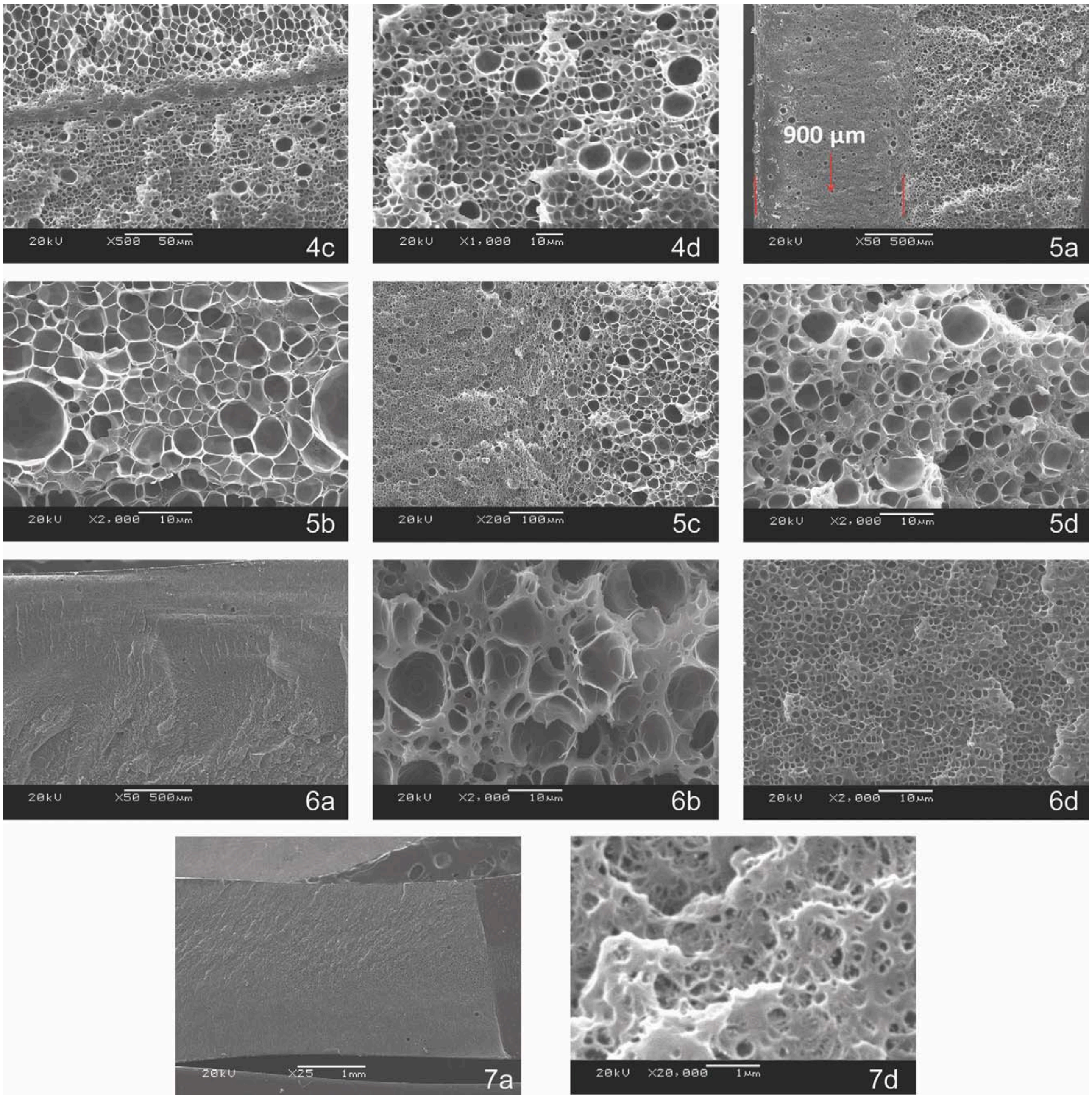

Figure 11. Continued

determined to be 5 MPa at 25°C. Sorption of CO_2 in PET was measured using MSB and the diffusivity determined by Fick's second law. The diffusion coefficient of CO_2 in PET was determined to be 6.7×10^{-13} m^2/s at 25°C and the CO_2 pressure of 6 MPa. The least critical CO_2 concentration for CO_2-induced crystallization was 9.17 wt % in PET at 25°C. A model coupling CO_2 diffusion in and CO_2-induced crystallization of PET was proposed to calculate the CO_2 concentration as well as crystallinity distributions in PET at different saturation times. A sandwich crystallization structure was found in the PET sheet at an appropriate saturation time, based on which a solid-state foaming process was used to control sandwich-structure of PET foams with two microcellular or ultra-microcellular foamed crystalline layers outside and a microcellular foamed amorphous layer inside. The thickness of the foamed-crystalline layer agreed well with that calculated by the model. At the saturation time as long as possible, PET ultra-microcellular foams with average bubble size of 193 nm and bubble density of 3.37×10^{13} could be fabricated.

Table 2. Comparison of the Evolution of Crystalline Layer Thickness Calculated Using the Model Coupling CO_2 Diffusion and Induced Crystallization and in PET Foams

Saturation Time (Day)	1	2	3	5	7
Thickness of crystalline layer (μm)					
In PET foams	0*	80	130	250	900
Modeling	20	50	100	300	Complete

*The crystalline layer was not detected in the PET foams due to the overlap of crystalline and the un-foamed skin layer of the PET specimen.

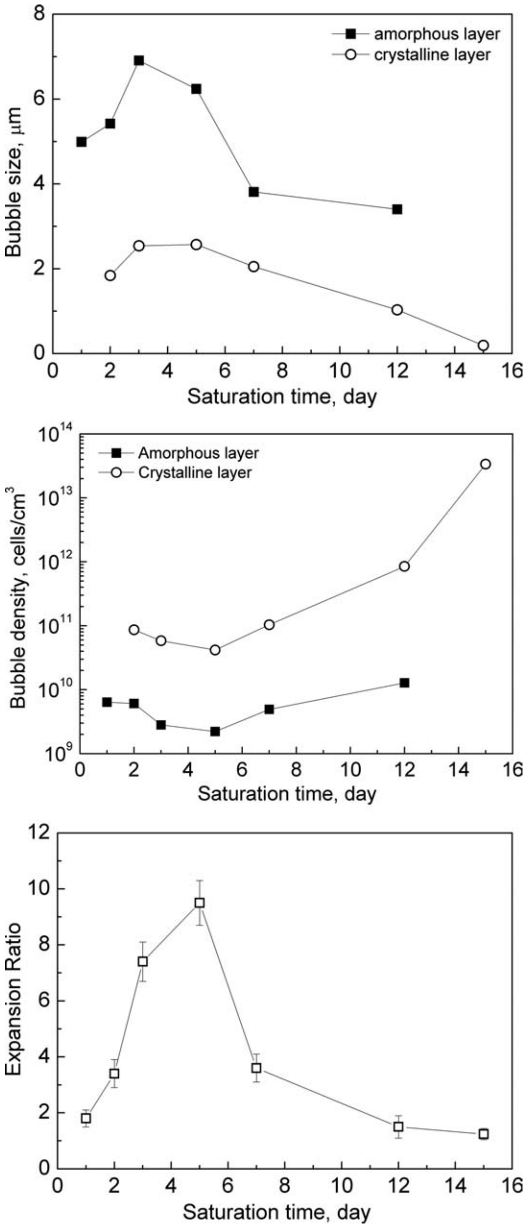

Figure 12. Characterization of the PET foams obtained at different saturation time.

The lines only indicate the trend.

Acknowledgments

The authors are grateful to the National Natural Science Foundation of China (Grant No. 20976045 and 20976046), Shanghai Shuguang Project (08SG28), Program for New Century Excellent Talents in University (NCET-09-0348), Innovation Program of Shanghai Municipal Education Commission (11CXY23), Program for Changjiang Scholars and Innovative Research Team in University (IRT0721), the 111 Project (B08021), and the support of "the Fundamental Research Funds for the Central Universities."

Literature Cited

1. Sorrentino L, Di Maio E, Iannace S. Poly(ethylene terephthalate) foams: correlation between the polymer properties and the foaming process. *J Appl Polym Sci*. 2010;116:27–35.
2. Mark JE. *Polymer Data Handbook*. London: Oxford University Press, 1999.
3. Martini JE. The Production and Analysis of Microcellular Foam (Master Thesis). Department of Mechanical Engineering, Massachusetts Institute of Technology, Cambridge, MA, 1981.
4. Martini JE, Suh NP, Waldman FA. Microcellular closed cell foams and their method of manufacture. 1982. US Patent 4,473,665.
5. Shen J, Han X, Lee LJ. Nanoscaled reinforcement of polystyrene foams using carbon nanofibers. *J Cell Plast*. 2006;42:105–126.
6. Han X, Koelling KW, Tomasko DL, Lee LJ. Continuous microcellular polystyrene foam extrusion with supercritical CO_2. *Polym Eng Sci*. 2002;42:2094–2106.
7. Krause B, Mettinkhof R, Van der Vegt NFA, Wessling M. Microcellular foaming of amorphous high-T_g polymers using carbon dioxide. *Macromolecules*. 2001;34:874–884.
8. Sun H, Mark JE. Preparation, characterization, and mechanical properties of some microcellular polysulfone foams. *J Appl Polym Sci*. 2002;86:1692–1701.
9. Huang Q, Klötzer R, Seibig B, Paul D. Extrusion of microcellular polysulfone using chemical blowing agents. *J Appl Polym Sci*. 1998;69:1753–1760.
10. Krause B, Sijbesma HJP, Münüklü P, Van der Vegt NFA, Wessling M. Bicontinuous nanoporous polymers by carbon dioxide foaming. *Macromolecules*. 2001;34:8792–8801.
11. Krause B, Diekmann K, Van der Vegt NFA, Wessling M. Open nanoporous morphologies from polymeric blends by carbon dioxide foaming. *Macromolecules*. 2002;35:1738–1745.
12. Kumar V. Polyethylene terephthalate foams with integral crystalline skins. 1993. US Patent 5,223,545.
13. Baldwin DF, Shimbo M, Suh NP. The Role of gas dissolution and induced crystallization during microcellular polymer processing—a study of poly(ethylene-terephthalate) and carbon-dioxide systems. *J Eng Mater Technol*. 1995;117:62–74.
14. Baldwin DF, Park CB, Suh NP. A microcellular processing study of poly(ethylene terephthalate) in the amorphous and semicrystalline states .1. Microcell nucleation. *Polym Eng Sci*. 1996;36:1437–1445.
15. Baldwin DF, Park CB, Suh NP. A microcellular processing study of poly(ethylene terephthalate) in the amorphous and semicrystalline states. 2. Cell growth and process design. *Polym Eng Sci*. 1996;36: 1446–1453.
16. Kumar V, Schirmer H. Semi-continuous production of solid state polymeric foams. 1997. US Patent 5,684,055.
17. Kumar V, Juntunen RP, Barlow C. Impact strength of high relative density microcellular CPET foams produced by the solid-state process using CO_2 as a blowing agent. *Foams '99: First International Conference on Thermoplastic Foam,* New Brunswick, NJ, 1999:157–164.
18. Kumar V, Juntunen RP, Barlow C. Impact strength of high relative density solid state carbon dioxide blown crystallizable poly (ethylene terephthalate) microcellular foams. *Cell Polym*. 2000;19: 25–37.
19. Guan R, Wang BQ, Lu DP. Preparation of microcellular poly(ethylene terephthalate) and its properties. *J Appl Polym Sci*. 2003;88:1956–1962.
20. Guan R, Wang BQ, Lu DP, Fang Q, Xiang BL. Microcellular thin PET sheet foam preparation by compression molding. *J Appl Polym Sci*. 2004;93:1698–1704.
21. Guan R, Xiang BL, Xiao ZX, Li YL, Lu DP, Song GW. The processing-structure relationships in thin microcellular PET sheet prepared by compression molding. *Eur Polym J*. 2006;42:1022–1032.
22. Li DC, Liu T, Zhao L, Yuan WK. Solubility and diffusivity of carbon dioxide in solid-state isotactic polypropylene by the pressure decay method. *Ind Eng Chem Res*. 2009;48:7117–7124.
23. Tomasko DL, Li H, Liu D, Han X, Wingert MJ, Lee LJ, Koelling KW. A review of CO_2 applications in the processing of polymers. *Ind Eng Chem Res*. 2003;42:6431–6456.
24. Li Y, Xiang B, Liu J, Guan R. Morphology and qualitative analysis of mechanism of microcellular PET by compression moulding. *Mater Sci Tech-Lond*. 2010;26:981–987.
25. Jacobs LJM, Kemmere MF, Keurentjes JTF, Mantelis CA, Meyer T. Temperature-induced morphology control in the polymer-foaming process. *AIChE J*. 2007;53:2651–2658.
26. Goel SK, Beckman EJ. Nucleation and growth in microcellular materials—supercritical CO_2 as foaming agent. *AIChE J*. 1995;41:357–367.
27. Li DC, Liu T, Zhao L, Lian XS, Yuan WK. Foaming of poly(lactic acid) based on its nonisothermal crystallization behavior under compressed carbon dioxide. *Ind Eng Chem Res*. 2011;50:1997–2007.
28. Chow TS. Molecular interpretation of the glass transition temperature of polymer-diluent systems. *Macromolecules*. 1980;13:362–364.
29. Handa YP, Zhang Z, Wong B. Effect of compressed CO_2 on phase transitions and polymorphism in syndiotactic polystyrene. *Macromolecules*. 1997;30:8499–8504.
30. Zhang Z, Handa YP. An in situ study of plasticization of polymers by high-pressure gases. *J Polym Sci Part B: Polym Phys*. 1998;36:977–982.

31. Takada M, Hasegawa S, Ohshima M. Crystallization kinetics of poly(L-lactide) in contact with pressurized CO_2. *Polym Eng Sci*. 2004;44:186–196.
32. Lambert SM, Paulaitis ME. Crystallization of poly(ethylene terephthalate) induced by carbon dioxide sorption at elevated pressures. *J Supercrit Fluid*. 1991;4:15–23.
33. Mizoguchi K, Hirose T, Naito Y, Kamiya Y. CO_2-induced crystallization of poly(ethylene terephthalate). *Polymer*. 1987;28:1298–1302.
34. Eaves D. *Handbook of Polymer Foams*. Shrewsbury: Rapra Technology Limited, 2004.
35. Brantley NH, Kazarian SG, Eckert CA. In situ FTIR measurement of carbon dioxide sorption into poly(ethylene terephthalate) at elevated pressures. *J Appl Polym Sci*. 2000;77:764–775.
36. Kalospiros NS, Astarita G, Paulaitis ME. Coupled diffusion and morphological change in solid polymers. *Chem Eng Sci*. 1993;48:23–40.
37. Jiang XL, Liu T, Xu ZM, Zhao L, Hu GH, Yuan WK. Effects of crystal structure on the foaming of isotactic polypropylene using supercritical carbon dioxide as a foaming agent. *J Supercrit Fluid*. 2009;48:167–175.
38. Muschiatti LC. High melt strength PET polymers for foam application and methods relating thereto. 1993. US Patent 5,229,432.
39. Subramanian PM, Tice CL. Melt fabrication of foam articles. 1992. US Patent 5,128,202.
40. 3Acomposites. http://www.corematerials.3acomposites.com/america.html. Accessed on September 6, 2011
41. Armacell. http://www.armacell-core-foams.com/ Accessed on September 6, 2011.
42. Li L, Liu T, Zhao L, Yuan WK. CO_2-induced crystal phase transition from Form II to I in isotactic poly-1-butene. *Macromolecules*. 2009;42:2286–2290.
43. Sato Y, Takikawa T, Takishima S, Masuoka H. Solubilities and diffusion coefficients of carbon dioxide in poly(vinyl acetate) and polystyrene. *J Supercrit Fluid*. 2001;19:187–198.
44. Lei ZG, Ohyabu H, Sato Y, Inomata H, Smith RL Jr. Solubility, swelling degree and crystallinity of carbon dioxide-polypropylene system. *J Supercrit Fluid*. 2007;40:452–461.
45. Sato Y, Takikawa T, Sorakubo A, Takishima S, Masuoka H, Imaizumi M. Solubility and diffusion coefficient of carbon dioxide in biodegradable polymers. *Ind Eng Chem Res*. 2000;39:4813–4819.
46. Sato Y, Takikawa T, Yamane M, Takishima S, Masuoka H. Solubility of carbon dioxide in PPO and PPO/PS blends. *Fluid Phase Equilib*. 2002;194–197:847–858.
47. Lee WH, Ouyang H, Shih MC, Wu MH. Kinetics of solvent-induced crystallization of poly(ethylene terephthalate) at the final stage. *J Polym Res-Taiwan*. 2003;10:133–137.
48. Keum JK, Kim J, Lee SM, Song HH, Son YK, Choi JI, Im SS. Crystallization and transient mesophase structure in cold-drawn PET fibers. *Macromolecules*. 2003;36:9873–9878.
49. Zhang Y, Lu YL, Duan YX, Zhang JM, Yan SK, Shen DY. Reflection-absorption infrared spectroscopy investigation of the crystallization kinetics of poly(ethylene terephthalate) ultrathin films. *J Polym Sci Part B: Polym Phys*. 2004;42:4440–4447.
50. Qian R, Shen D, Sun F, Wu L. The effects of physical ageing on conformational changes of poly(ethylene terephthalate) in the glass transition region. *Macromol Chem Phys*. 1996;197:1485–1493.
51. Avrami M. Kinetics of phase change. I. General theory. *J Chem Phys*. 1939;7:1103–1112.
52. Avrami M. Kinetics of phase change. II. Transformation-time relations for random distribution of nuclei. *J Chem Phys*. 1940;8:212–224.
53. Avrami M. Kinetics of phase change. III. Granulation, phase change, and microstructure. *J Chem Phys*. 1941;9:177–184.
54. Run M, Hao Y, Yao C. Melt-crystallization behavior and isothermal crystallization kinetics of crystalline/crystalline blends of poly(ethylene terephthalate)/poly(trimethylene terephthalate). *Thermochim Acta*. 2009;495:51–56.
55. Wellen RMR, Rabello MS. Antinucleating action of polystyrene on the isothermal cold crystallization of poly(ethylene terephthalate). *J Appl Polym Sci*. 2009;114:1884–1895.
56. Deshpande VD, Jape S. Isothermal crystallization kinetics of anhydrous sodium acetate nucleated poly(ethylene terephthalate). *J Appl Polym Sci*. 2010;116:3541–3554.
57. Crank J. *The Mathematics of Diffusion*, 2nd ed. London: Oxford University Press, 1975.
58. McGonigle EA, Liggat JJ, Pethrick RA, Jenkins SD, Daly JH, Hayward D. Permeability of N_2, Ar, He, O_2, and CO_2 through biaxially oriented polyester films—dependence on free volume. *Polymer*. 2001;42:2413–2426.
59. Lewis ELV, Duckett RA, Ward IM, Fairclough JPA, Ryan AJ. The barrier properties of polyethylene terephthalate to mixtures of oxygen, carbon dioxide, and nitrogen. *Polymer*. 2003;44:1631–1640.

Manuscript received June 2, 2011, and revision received Aug. 11, 2011.